Quantitative elemental analysis with the LMS-GT; a next-generation LIMS-TOF instrument

Coenraad P. de Koning[*], Salome Gruchola, Andreas Riedo, Reto Wiesendanger, Valentine Grimaudo, Rustam Lukmanov, Niels F.W. Ligterink, Marek Tulej, Peter Wurz

Physics Institute, Space Research and Planetary Sciences, University of Bern, Sidlerstrasse 5, CH-3012, Bern, Switzerland

ARTICLE INFO

ABSTRACT

Laser ablation is a highly suitable and widely applied technique for direct sampling of solid materials. The Laser Mass Spectrometer − Gran Turismo (LMS-GT), a Femtosecond Laser Ablation Ionization Time-of-Flight Mass Spectrometer with a mass resolution exceeding 10,000 (m/Δm at full-width half-maximum), was recently developed at the University of Bern with the aim of minimizing isobaric interferences and consequently improving the performance of the LIMS measurement technique for the quantification of the chemical composition of solids. To assess the quantitative performance of LMS-GT, mass spectrometric analysis four standard reference materials was conducted. The presented study shows that the achieved mass resolution of up to 12,000 is accompanied by high mean mass accuracy better than 10 ppm, with some elements displaying a deviation up to 100 ppm. Combined, these instrumental characteristics minimize isobaric interferences, which aids in confident identification and quantification of the chemical composition of solids. Limits of detection in the ppb-range and a linear dynamic range of over six orders of magnitude were achieved. Relative sensitivity coefficients were determined to lie between 0.5 and 5 for elements unaffected by loss of signal amplification with respect to the published values for bulk abundances. The lateral resolution of several micrometers achieved with LMS-GT allowed information on sample homogeneity at a micrometer scale to be acquired, with several elements (e.g., Mg, S, and Ca) showing variations in local abundances spanning a full order of magnitude. The combination of detection sensitivity, high mass resolution, and lateral resolution at the single-digit micrometer scale (down to ~2 μm) gives the LMS-GT the potential to be an interesting analytical tool for element analysis of solid samples, and represents a step forward for laser ablation ionization mass spectrometry as a measurement technique. However, steps to ensure a smaller range in relative sensitivity values, e.g., switching to UV laser irradiation, are required to further enhance the quantitative performance of this instrument, especially the event that no reference material is available for quantification.

© 2021 Published by Elsevier B.V.

1. Introduction

Sensitive and accurate quantitative multi-element analysis of solid samples represents an essential and ubiquitous part of many scientific and industrial fields. Examples include material [1], planetary [2,3], archaeological [4], and geological sciences as well as the semiconductor industry [5,6] and the art sector. Over the last decades, direct analysis of solid samples has become an increasingly attractive alternative to traditional methods, e.g., Thermal Ionization Mass Spectrometry (TIMS), Inductively-Coupled Plasma Mass Spectrometry (ICP-MS), Glow Discharge Mass Spectrometry (GDMS), and Spark Source Mass Spectrometry (SSMS), all of which involve extensive and laborious sample preparation steps such as digestion, dissolution, nebulization, evaporation, etc. Another highly successful technique is Secondary Ion Mass Spectrometry (SIMS), which is widely applied in the area of isotope research. It is capable of highly sensitive investigation at nanometer scales, allowing for mass spectrometric imaging with very high spatial resolution. However, even in the most advanced multi-collector (nano)SIMS systems, only a limited set of isotopes can be detected simultaneously. For many natural samples, this constitutes a limitation, since it might limit the investigation of a single

microscopic inclusion to a limited number of elements and/or isotope systems. Furthermore, quantitative information on element abundances cannot be provided by SIMS.

With the emergence of stable and affordable short (femto-second, picosecond, and nanosecond) pulsed laser systems, laser ablation has proven to be a highly suitable technique for direct sampling of a wide range of solid sample materials [7,8]. A major advantage of solid sampling by means of laser ablation is the micrometer scale lateral and nanometer scale vertical resolution that can be achieved, allowing for mapping and imaging of element distributions throughout sample material. Several analytical techniques making use of laser ablation for solid sample analysis have been developed over the last decades, the most widely applied are Laser Ablation Inductively Coupled Plasma Mass Spectrometry (LA-ICP-MS) and Laser-Induced Breakdown Spectroscopy (LIBS) [9,10]. Both techniques have their advantages and drawbacks [11,12], making them suitable for different applications.

The main advantages of LIBS are its relative simplicity and portability [13], the possibility of doing stand-off measurements without requiring sample preparation (which increases its ease-of-use and reduces the chance of contamination), and its compatibility with other spectroscopic techniques such as Raman spectroscopy. However, LIBS is typically described as being only semi-quantitative due to matrix effects, as well as having limited detection sensitivity compared to mass spectrometric techniques [11]. In contrast, LA-ICP-MS is a highly sensitive and quantitative measurement technique with detection limits at the ppb level [14–16]. These characteristics have made LA-ICP-MS a highly popular and widely used measurement technique for solid sampling. However, LA-ICP-MS occasionally suffers from non-stoichiometric processes originating from different sources, including matrix-dependent ablation rates, preferential transportation of sample material from the LA cell to the ICP plasma volume, and differences in ionization efficiency within the ICP [12]. Hybrid systems exist today that couple the advantages of both LIBS and LA-ICP-MS in one instrument [17–19].

The third member in the family of laser-based solid sampling techniques is Laser Ablation Ionization Mass Spectrometry (LIMS), consisting of both Laser Ablation (LA) and Laser Desorption (LD) methods. Using the applied laser pulses for both ablation and ionization results in a simplistic setup. The technique has been shown to be highly suitable for sampling very small volumes with high sensitivity [20–23]. This is especially true for LA methods when applying ultra-short laser pulses (i.e., fs-pulses) as the irradiation source, since, under these conditions, LIMS can be expected to rely less on matrix-matched standards [24–26].

One of the main strengths of laser ablation for solid sampling is the possibility to acquire information on both lateral and vertical distribution and variation of elements throughout a sample. The resolution is directly related to the laser spot dimension and applied laser fluence. Lateral and vertical resolution are important figures of merit for targeted investigation of micro- or nanoscale structures. Brinckerhoff et al. reported a laser spot diameter of ~30 − 50 μm for the Laser Ablation Mass Spectrometer (LAMS), a LIMS instrument designed for space application with a vertical resolution of 200 - 300 nm per shot [3]. A lateral resolution of 80 nm and ablation rate of 13 − 70 nm per shot was reported for the EUV-TOF instrument by Green et al. [23] Grimaudo et al. recently reported a vertical resolution of ~30 nm[21] by employing a sophisticated UV double pulse post-ionization operation mode, while achieving a lateral resolution of ~10 μm [27].

Due to the pulsed nature of a laser ablation ion-source, Time-of-Flight (TOF) type mass analyzers are especially suitable for LIMS analysis and are therefore widely applied in LIMS instruments. The wide range of initial kinetic energies resulting from the ablation process means that the mass resolution (defined as m/Δm at full-width half-maximum (FWHM)) achievable by LIMS-TOF systems is typically limited to ~1,000 − 2,000 [23,28–31].

However, as with all mass spectrometric techniques used for element analysis, analysis of LIMS data is often complicated due to isobaric interferences, which are common due to the presence of polyatomic (molecular) and multiply charged species formed in the laser-induced plasma plume [10]. Currently, isobaric interferences are typically unresolvable by most LIMS-TOF systems due to the insufficient mass resolution of the mass analyzer systems, which impedes accurate element and isotope quantification [7,20,32,33].

One possible way to address this challenge is the use of a different type of mass analyzer, such as an Orbitrap, as used in the LAb-CosmOrbitrap instrument [34,35]. This instrument has been reported to achieve mass resolutions exceeding the requirements for resolving most isobaric interferences (m/Δm > 100,000). However, one drawback of the CosmOrbitrap is its limited sensitivity (detection limits in the per mill range) compared to LIMS-TOF instruments [36,37] and dynamic range [37]. A second example of the use of a different (high resolution) mass analyzer is the coupling of LIMS (typically Laser Desorption) to a Fourier transform ion cyclotron resonance (FT-ICR) mass analyzer. Similarly high mass resolutions have been shown for LD FT-ICR instruments, with mass resolutions above 100,000 reported by different groups [38–40]. However, due to the different ionization technique, quantitative analysis is highly challenging.

Recently, the Laser Mass Spectrometer "Gran Turismo" (LMS-GT), a novel laboratory-scale LIMS system, was constructed at the University of Bern. The instrument was designed specifically to combine the high detection sensitivity of LIMS-TOF instrumentation with a mass resolution sufficient to address the issue of isobaric interferences between polyatomic, monoatomic, and multiply charged species. An extensive description of the design of the LMS-GT was published recently by Wiesendanger et al. [41] Preliminary data showed good detection sensitivity (ppm level) and high mass resolution (m/Δm at FWHM exceeding 10,000). However, preliminary quantitative analysis was performed only for NIST SRM 664, where merely twelve laser ablation craters were analyzed per sample. Due to the level of chemical heterogeneity present in the investigated sample material and the limited amount of sample material subjected to analysis, the influence of certain system and sample characteristics on the (quantitative) performance of the LMS-GT could not be assessed by Wiesendanger et al.

In this study, the capability of LMS-GT to conduct accurate quantitative analysis will be assessed in detail through a large scale investigation of four different metal Standard Reference Materials (SRM). Additionally, the influence of several instrumental parameters on quantitative performance will be investigated. The assessment will include different aspects of quantitative analysis, including the necessity for acquisition with high dynamic range, the influence of the high mass resolution mass analyzer on data analysis, as well as the role of sample (in)homogeneity.

2. Experimental

2.1. LMS-GT

An extensive description of the technical design of the LMS-GT was given in an earlier publication [41]. Therefore, only a short overview of the main components will be given here. A summary of the key instrument and operation parameters is given in Table 1. The LMS-GT is a Laser Ablation Ionization instrument coupled to a TOF mass analyzer, capable of performing solid sample investigation with a lateral resolution of ~2 μm. The sample holder, sample, and mass analyzer are housed within a stainless steel vacuum

Table 1
Key instrumental/operational parameters.

Characteristic	Value
Laser	
Wavelength	775 nm
Pulse duration	~190 fs
Repetition rate	1 kHz
Pulse energy	$0.01 - 1$ mJ
Energy stability	4-8‰
Mass spectrometer	
Lateral resolution	~2-8 μm
Laser power density (typical)	$\sim 5 - 20$ TW cm^{-2}
Mass resolution (typical)	$5,000 - 10,000$
Base pressure	~1-2 [a] 10-8 mbar
Time-of-flight path length	~ 4 m
Time-of-flight ($1 - 200$ m/z)	~ $5 - 80$ μs
Digitization	
ADC Sampling rate	3.2 GS/s
Vertical resolution	12-bit
Bandwidth	$DC - 2$ GHz
Measurement procedure	
Analyzed locations per sample	50
Applied pulses per location	38,400[a]
Acquired TOF length	100 μs

[a] Stored as 400 spectra, each a histogram of 96 single-laser-pulse spectra.

chamber (0.75 x 0.75 × 0.75 m^3). During measurements, the pressure in the vacuum chamber is kept at UHV conditions, $(1 - 2) * 10^{-8}$ mbar, at all times by a turbomolecular pumping system (HiPace 700 M, Pfeiffer Vacuum AG, Switzerland) backed up by a scroll pump (ACP 15 SD, Pfeiffer Vacuum AG, Switzerland). The sample holder is attached to an x-y-z translation stage, which, in combination with an in-line microscope camera system, allows for real-time targeting of specific features on a sample with micrometer accuracy as well as on-line visualization of ablation craters.

A Clark-MXR CPA Ti:sapphire laser system ($\lambda = 775$ nm, ~190 fs, 1 kHz) connected to the mass spectrometer was used as the laser ablation ionization source. This laser system generates a pulsed laser beam with pulse energies up to 1 mJ and high pulse-to-pulse stability (~4−8‰ measured as the standard deviation of 20,000 pulses, i.e., 20 s of continuous output at 1 kHz). The pulsed laser beam is guided towards the sample by the laser optical system, comprising four fold mirrors, a beam expander, a specially designed fold mirror with a central borehole, and a Schwarzschild-type two-mirror objective, which focuses the pulsed laser beam onto the sample surface.

Each laser pulse impinging onto the sample surface ablates and ionizes a thin layer of material, producing a plasma plume. The ion-optical system extracts the positive ions from the plasma plume and separates them based on the TOF principle. The ion-optical system comprises an ion source for extraction and acceleration, three electrostatic lenses for refocusing of the ion beam, and two gridless ion mirrors for correction of differences in initial ion velocity. The total length of the twice-folded ion flightpath is ~4 m.

Ions are detected using a MagneTOF detector (ETP, Australia). Contrary to more traditionally used multi-channel plate (MCP) detectors, the MagneTOF detector contains a full metal multiplier, which allows much faster recharging after (partial) depletion by an intense ion packet. In turn, this allows for acquisition at high repetition rates (1 kHz) without depletion of electrons from the detector (and consequential loss of signal amplification) between consecutive laser pulses.

In contrast to the study presented by Wiesendanger et al. (2019), which employed an Acqiris U1084a (8-bit vertical resolution, sampling rate of 2 GS/s), in this study the acquisition of the signal was performed by an next generation Acqiris U5303a ADC-card (12-bit vertical resolution, 3.2 GS/s, DC- 2 GHz bandwidth), hosted in a dedicated measurement computer. The higher vertical resolution of the currently used ADC-card, the electronic dampening of the signal lines against specific oscillations observed during initial measurements, and the low intrinsic noise of the measurement setup should allow for acquisition with higher dynamic range and improved limits of detection compared to the study presented by Wiesendanger *et al* (2019).

2.2. Samples

To assess the capabilities of the LMS-GT for quantitative element analysis of solids, four metal SRMs were selected based on their compatibility with laser ablation by an infrared 775 nm laser source and the size of heterogeneities known to be present in the material: steel NIST SRM 661, high-carbon steel NIST SRM 664, and high-purity electrolytic iron NIST SRM 665, and a Cu−Ni alloy named BCS-SRM 180/2 from the Bureau of Analyzed Samples Ltd. (BAS). Certified quantitative information on the elemental make-up of the samples is provided in the SRM certificate of analysis. For the samples provided by NIST, each certificate also provides estimate abundances for a group of elements, which are typically only reported on by a single measurement technique and thus not certified. Both certified and estimated values were used during this study to assess the quantitative performance of LMS-GT, though more significance should be attributed to the certified values. The certificates provided by the BAS only state certified abundances. The NIST SRM samples were previously used as testbed to show preliminary functionality and performance as reported by Wiesendanger et al. (2019).

To remove the contamination layer on the surface (e.g., from oxidation or sample handling), samples were manually polished with increasingly fine-grained sanding paper and ultrasonically cleaned in high purity isopropanol and high purity acetone for 15 min. Samples were then rinsed using ultra-pure water (>18 MΩ cm^{-1}) and dried first under ultrapure N_2 flow (Alphagas, $N_2 \geq 99.999\%$, Carbagas, Switzerland) for $1−2$ min, and further dried under high vacuum conditions (10^{-6} mbar) for 30 min.

As a final step, samples were cleaned using an ion sputter gun (Tectra GmbH, Physikalische Instrumente, Germany) using high-purity argon (Carbagas, Switzerland). The ion gun was operated at ~3 keV with an angle of incidence of ~10° for 30 min. Subsequently, the samples were introduced into the vacuum chamber of LMS-GT, which was pumped down to ~2 · 10^{-8} mbar.

2.3. Measurement procedure

The in-line optical microscope camera system was used to position the sample in the focal plane of the laser beam, which was verified by the characteristics (size, shape, sharpness of edges) of the ablation crater. Optima in laser power and ion-optical settings were determined manually based on ion transmission (i.e., signal intensity) and spectral resolution for the complete mass range during an initial campaign on NIST SRM 664. The selected optimal laser energy was 11.4 μJ per pulse before transmission losses, equaling roughly 570 nJ after transmission losses and, correspondingly, an irradiance of 6.4 TW/cm^2, which was used for all three samples. The detector voltage was set to 2,150 V, which allowed for visual confirmation of the presence of peaks corresponding to elements at the trace level during the recording of TOF spectra. A measurement campaign applying detector voltages ranging from 1,900 V to 2,150 V was conducted on NIST SRM 664 to ensure the detector was operated within its linear dynamic range operating window (results can be found in the Supplementary Information).

Fifty locations, arranged in a rectangular raster of five-by-ten locations (x-pitch: 100 μm, y-pitch: 50 μm), were analyzed on each sample. Accordingly, the analysis was conducted on a total area of 0.18 mm², in order to minimize the effects of local heterogeneity. A total of 38'400 laser pulses were applied to each sample location at a laser pulse repetition rate of 1 kHz. A full TOF spectrum of 100 μs was recorded for each applied laser pulse. Real-time histogramming of 96 consecutive single laser shot spectra was performed on board of the ADC-card before writing a single histogrammed spectrum to the storage disk of the host computer, resulting in 400 spectra per sample location. Accordingly, a total of 20,000 spectra, representing 1,920,000 single laser shot spectra, were stored for each sample.

Based on previous studies by Grimaudo et al. using the same laser system, the mean material uptake rate at the applied irradiances can be expected to lay in the range of several picograms per applied laser pulse [5]. At these uptake rates, the total amount of analyzed material per layer (i.e., 96 laser pulse spectra histogrammed to a single spectrum) could be roughly estimated to lay in the range of hundreds of picograms, corresponding to a total of several hundred nanograms per sample location. At these quantities of analyzed material, chemical analysis of micrometer-scale features is possible.

To investigate the dependence of the quantitative performance on several instrument and sample parameters, additional measurements were performed. Firstly, a campaign was performed on the Cu−Ni alloy BCS-CRM 180/2 sample. Different pulse energies, ranging from 0.4 to 1.13 μJ (after transmission losses), were applied with the aim to gain information on the influence of matrix as well as the applied laser pulse energy. The detector voltage for this measurement campaign was 2,100 V.

Analysis of the datasets was performed using software written in MATLAB®, which was designed and produced in house specifically for analysis of LIMS-TOF data [42]. TOF spectra were converted to mass spectra according to the equation: $m(t) = k_0(t - t_0)$ [2], with m being the mass in atomic mass units, t the TOF in seconds, and k_0 and t_0 internal calibration constants. For the sake of consistency, the conversion from TOF spectrum to mass spectrum was calibrated on the same isotope peaks for all samples, which were: [10]B, [11]B, ^{13}C, ^{16}O, [27]Al, [30]Si, ^{31}P, [32]S, [63]Cu, [65]Cu, [93]Nb, and [100]Mo. All analysis was performed on raw data. Small modifications had to be made to the software to adapt it to the data produced by LMS-GT (narrower peaks and different baseline characteristics). To achieve the highest possible analytical accuracy, the first and last 100 spectra from each location were omitted from analysis, since these spectra typically suffer from processes such as crater formation and residual surface contamination and oxidation.

3. Results and discussion

3.1. Spectral characteristics

Mass resolution. In accordance with a previous publication covering LMS-GT, the maximum mass resolution (measured as m/Δm at FWHM) achieved during this study was roughly 12,000 (measured at [90]Zr), with a mean mass resolution of around 9,000 for all identified monoatomic species (see Wiesendanger et al. 2019 for further details on the dependence of mass resolution on isotope mass) [41]. This constitutes roughly a 10% increase in both maximum and mean mass resolution observed in a previous study on the same metal samples, which can most likely be attributed to optimizations in applied laser power [41]. Mass peaks produced at these mass resolutions are only several ns wide, and suffer slightly from under-sampling at the current sampling rate of 3.2 GS/s. Therefore, the mass resolution is expected to improve when using a

data acquisition system with a higher sampling rate and bandwidth.

As mentioned before, high spectral resolution has a number of distinct advantages, the most evident of which is that it makes it possible to resolve isobaric interferences between monoatomic, polyatomic, and multiply charged species. Resolving isobaric interferences directly facilitates quantification by increasing the number of peaks valid for integration. An example of this is shown in Fig. 1, where integration of the [14]N⁺ peak is possible only because it is fully baseline-separated from the [28]Si²⁺ peak. Note that since ^{15}N falls below current detection levels ([14]N:[15]N = 0.99636:0.00364 ≈ 274) [43] in all three NIST steel samples, element quantification of N depends fully on the ^{14}N isotope. A polyatomic species, [12]C−H₂, was anticipated due to the high carbon content of the steel, but, due to the high mass resolution and high mass accuracy, it can be confidently stated that this species was not observed.

The second advantage of high mass resolution is the reduced complexity of analysis. At high spectral resolution, the number of unresolvable isobaric interferences that can reasonably be expected to occur for a given sample is highly reduced compared to low spectral resolution. Accordingly, confident identification and subsequent quantification are simplified, since the necessity to investigate each possible isobaric interference and manually omit affected peaks from the analysis is minimized.

Mass accuracy. Confident assignment of peaks, which is especially crucial for accurate quantification of trace elements, is further facilitated by high accuracy of the mass scale. In TOF mass spectrometry, mass accuracy is inversely related to mass resolution, such that the average mass accuracy is expected to be approximately:

$$Mass\ accuracy = \frac{m_{det} - m_{true}}{m_{true}} \cong \frac{1}{MR*10}$$

where m_{det} is the determined mass of a peak, m_{true} is the true mass of the assigned species, and MR is the mass resolution. Fig. 2 shows the mass accuracy for all detected elements in each of the three NIST steel samples. With an average mass accuracy of 7.8 ppm, the
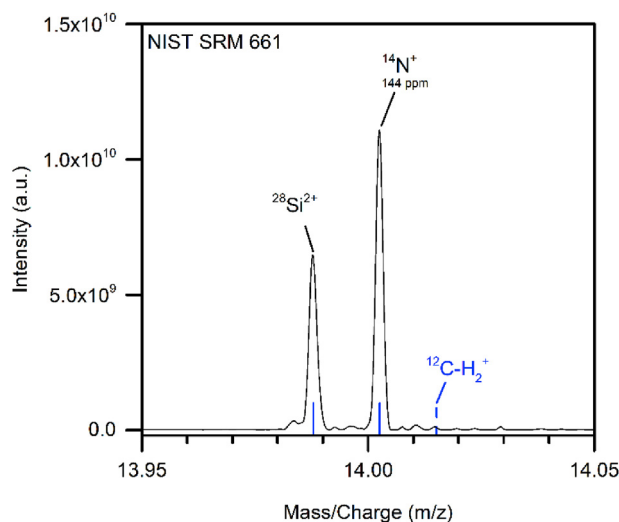
Fig. 1. Selected mass range from a spectrum acquired from NIST SRM 661. The abundance of ^{14}N is given as atomic fraction. Blue lines represent the true mass of the different species. CH₂ is a polyatomic (molecular) species, which could be expected to occur in high carbon steel but was not observed to be present.
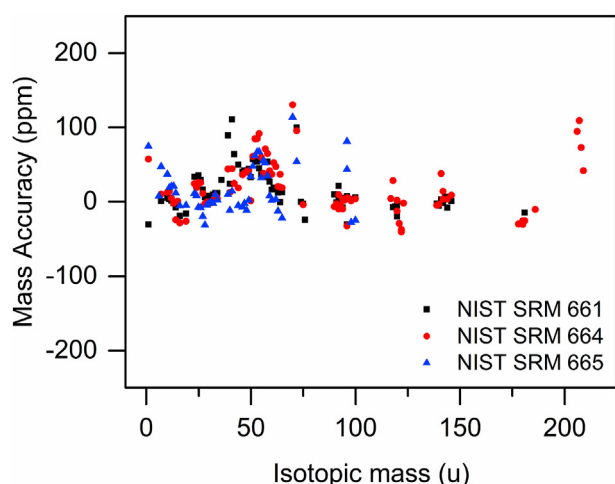
Fig. 2. Mean mass accuracies of all detected element isotopes for each of the three analyzed NIST SRM samples.

accuracy is in line with the expected value of ~11 ppm at a mean mass resolution of ~9,000.

As can be seen in Fig. 2, most points are randomly distributed around zero. However, there are two regions where a different trend can be observed. First, the elements between mass 50 and 60 seem to be shifted slightly upwards, meaning m_{det} is slightly higher than the m_{true}. Peaks of elements slightly lighter than ^{56}Fe (e.g., ^{51}V, ^{52}Cr, ^{55}Mn) are influenced similarly to peaks slightly heavier than ^{56}Fe (e.g., ^{59}Co), which might indicate that the cause of the higher m_{det} for these elements is related to electrostatic interactions or ion-optical issues. This is most likely also valid for the second group with a deviating mass accuracy containing the isotopes of lead and bismuth, although ion-optical issues seem the more likely reason here since highly intense ion packets, potentially causing electrostatic interaction, are not present near Pb and Bi in any of the recorded spectra. While there is some ringing after intense signals due to the inevitable minor impedance mismatches in the signal line, no effect on the mass accuracy of subsequent peaks was observed. High mass accuracy is especially beneficial when isotope patterns cannot be used to aid identification, i.e., for monoisotopic elements (e.g., Na, Al, P) and trace elements with one major isotope (e.g., La in the case of the analyzed samples). It is worth noting that at mass accuracies in the single-digit ppm range, the mass of the electron 'missing' from the detected cations needs to be taken into account to make correct assignments, as it constitutes a significant fraction of the total mass (e.g., ~11 ppm at the mass of ^{48}Ti).

Detection sensitivity. Another important figure of merit in instrument performance is the detection sensitivity. The preliminary analysis presented by Wiesendanger et al. showed high detection sensitivity down to the single-digit ppm level [41]. Owing to improvements in the acquisition system, such as an ADC card with higher vertical resolution and dampening of HV supply lines to the detector, the linear dynamic range of the instrument was expected to have increased. The resulting high detection sensitivity achieved during this study is exemplified in Fig. 3, where detection of several isotopes with abundances down to ppb levels is shown, such as ^{49}Ti, ^{141}Pr, and ^{144}Nd, with abundances of 380, 540, and 270 ppb atomic fraction (a.f.), respectively.

The detection of ^{44}Ca at an abundance of 28 ppb a.f. (Fig. 3c) constitutes a limit of detection two full orders of magnitude lower than previously published results [41]. Validation of this high detection sensitivity is only possible due to the combination of high mass resolution and mass accuracy. The achieved mass resolution
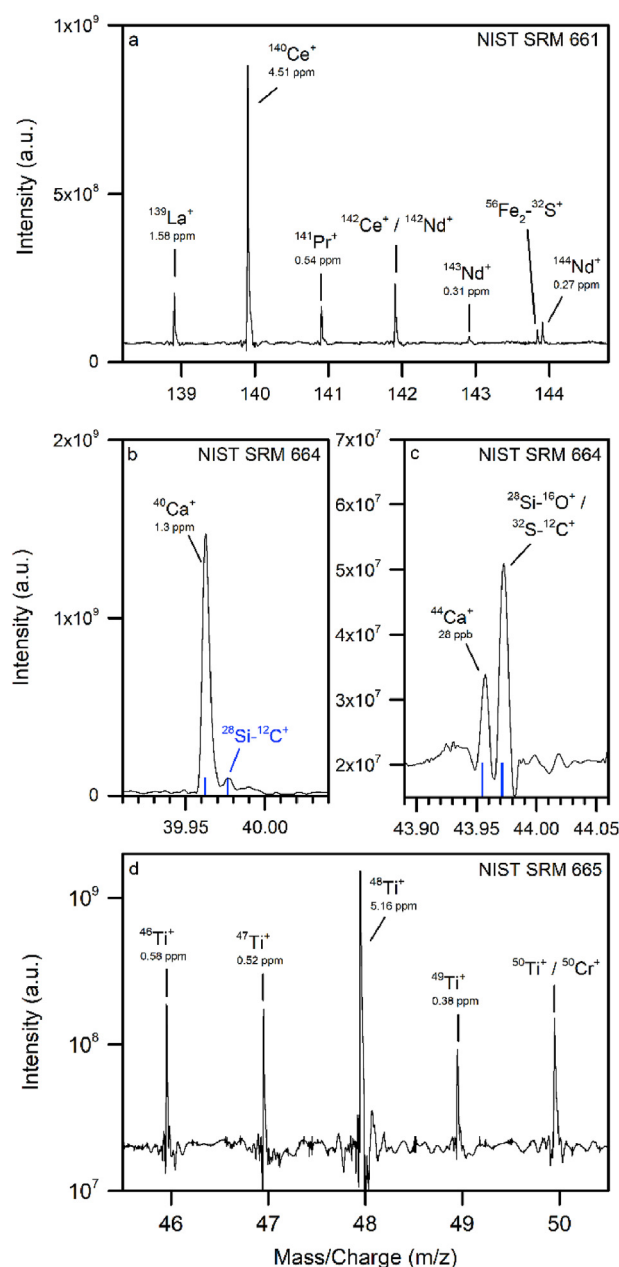

Fig. 3. Selected mass ranges from spectra acquired from the different analyzed NIST SRM steel samples. The blue lines in the middle panels represent the nominal mass of the assigned species. The assignment of Si−C in panel b cannot be made with absolute confidence as the observed peak might be due to ringing, which is why it is denoted in blue. Note the logarithmic scale on panel d.

allows for a distinction between the monoatomic Ca species and polyatomic species with a similar nominal mass, while the high mass accuracy allows for confident identification. In this case, the identification of Ca species is supported by the ^{40}Ca:^{44}Ca isotope ratio (96.941:2.086 ≈ 46.5)[43] being in line with the observed intensities for the assigned peaks.

The high sensitivity observed for Ca is partly due to its low first ionization energy. However, sub-ppm sensitivity was observed for elements with higher ionization energies as well. In Fig. 3d, Ti isotopes with sub-ppm abundances can clearly be observed. An estimation of the theoretical limit of detection can be made based on the observed signal-to-noise ratio (SNR) for species present at trace level abundances. For instance, ^{46}Ti is detected with an SNR of

~7 at an abundance of 580 ppb, meaning the theoretical limit of detection at a SNR of 1 is ~80 ppb for Ti. Isobaric interference of $^{46}Ca^+$ and $^{48}Ca^+$ with $^{46}Ti^+$ and $^{48}Ti^+$ is unlikely to be a significant factor in this detection, since the Ti:Ca ratio for these isotopes is relatively large (~100,000 and ~20,000 for ^{46}Ti:^{46}Ca and ^{48}Ti:^{48}Ca, respectively).

Note that the intensity of the $^{50}Ti^+$ (Fig. 3d) is higher than one would expect based on intensities of the other Ti peaks due to isobaric interference with $^{50}Cr^+$. Resolving this isobaric interference requires a mass resolution exceeding 100,000, which is beyond the capabilities of LMS-GT. However, no interferences are observed (or expected) for any of the other Ti isotopes, meaning the elemental abundance of Ti can still be measured accurately. Moreover, the separate contributions of ^{50}Ti and ^{50}Cr to the peak observed at m/z 50 can be determined to aid in the quantification of Cr and its isotopes.

3.2. Quantitative performance of LMS-GT

Measured abundances of elements. In the current setup, a discrete dynode electron multiplier, the ETP MagneTOF Plus detector, is used to record the ion signal. This detector is capable of detecting single ions up to large ion fluxes with a high linear dynamic range. Consequently, the recorded signal intensity is directly proportional to the number of ions detected. Thus, measuring the areas under the peaks (e.g., by integration) for one or several isotopes of a given element provides a direct measure for its relative abundance in the sample.

To calculate the relative abundance of an element from the measured areas under the peaks of its isotopes, a normalization step is required. Normalization to a single element, such as a major element present in the sample, is often performed. However, due to the substantial chemical inhomogeneity of the analyzed samples, as well as the inherent fluctuation of signal in non-averaged spectra, normalization to a single element would degrade the relative abundance determination. To overcome this issue, normalization was performed against the sum of areas under the peaks for all detected and identified monoatomic species present in the sample as specified by NIST. Only Fe was omitted from the normalization denominator, since its abundance is not certified in any of the NIST steel samples, and any deviation of its true abundance with respect to the abundance stated by NIST will have large effects on the normalization as it is the main constituent. As a result, the calculated abundance for a given element represents the number of ions detected for that element as a fraction of all ions of all identified monoatomic species detected in a spectrum except for Fe, rather than as a fraction of the number of ions detected for a single element of choice.

Fig. 4 shows the mean measured abundances of all detected and identified elements for each sample as a function of the element abundance as provided by NIST. Elements with certified element abundances are denoted with solid symbols, whereas elements which where only quantified with a single measurement technique are indicated with open symbols. Several analytical features are directly apparent from Fig. 4, such as the wide range of detectable elements, as well as the high detection sensitivity with elements down to 100 ppb a.f. being quantifiably detected in a single measurement. However, sensitivities for a number of elements deviate strongly from the mean, for example Mg, Ca, and Pb being higher, and As being lower.

One noteworthy aspect of Fig. 4 is the relatively low signal recorded for Fe in all three NIST steel samples. Since only the ^{54}Fe peak was used for quantification of Fe, detector gain loss and/or subsequent aberrant detector behavior is not expected to play a role in this observation. Furthermore, relatively low signal for Fe was observed in previous studies conducted on NIST SRM 661, 664, and 665 by our group (unpublished data). Several causes for the low Fe signal can be proposed, e.g., low specific ion-yield during ablation ionization, preferential neutralization of Fe ions in the ablation plume consisting mainly of iron, and/or a deviation of the true Fe abundance from the non-certified value listed by NIST. Moreover, several measurement parameters concerning, e.g., the detector, the ADC card, and the laser, were optimized with a focus on minor and trace elements, of which quantification is the objective of this work. This optimization process could contribute to a reduced signal for species with an abundance of >95% such as Fe in this case. Determining which of these factors contributes most significantly to the low recorded signal for Fe requires extensive investigation, and is beyond the scope of this study.

To correct for the different ion yields from the laser ablation ionization process, as well as different detection sensitivities for different elements, in order to provide an accurately quantified atomic concentration for the detected elements, application of relative sensitivity coefficients (RSCs) is required. The RSC value of an element of interest x is obtained as follows:

$$RSC = \frac{A_{x(measured)}}{A_{x(reference)}}$$

where $A_{x\,(measured)}$ stands for the measured atomic abundance for element x (calculated as described above), and $A_{x\,(reference)}$ represents its reference abundance. Using the RSCs as correction factors allows for accurate quantification when conducting measurements on unknown samples with similar matrix characteristics.

Fig. 5 shows RSC values calculated for all detected elements for each sample. While most elements lighter than Fe are detected with an RSC between 0.5 and 5, measurements of elements heavier than Fe suffer from the gain depletion of the detector by the high Fe intensities (approx. $300,000 - 400,000$ Fe ions). Due to depletion of electrons from the detector dynode plates by the highly intense Fe signal, and their recharging which exceeds the time to the following mass peaks, all species heavier than Fe suffer from a loss of signal amplification. Accordingly, all elements heavier than Fe have a systematically lower RSC (i.e., in all three NIST steel samples, the average RSC value for elements after Fe is roughly a factor two lower than the average value for elements before Fe). This is also visible in Fig. 4, where the majority of data points below the solid diagonal line belong to elements heavier than Fe. RSC values of elements unaffected by loss of signal amplification are comparable to those achieved previously by other instruments employing fs-laser systems [20,44−46].

The issue of loss of signal amplification can be addressed in several ways, the most straightforward being by applying a correction factor. For instance, by using the average RSC of all species after Fe as a correction factor, >80% of all detected elements fall within an RSC between 0.1 and 10. However, such a linear correction factor is likely to be an oversimplification of the processes occurring after detector gain loss because of depletion of charge from the detector after a large peak. More likely, the recharging of the detector dynodes following charge depletion is exponential in time. To find an appropriate correction factor, accurate quantification of the loss of signal amplification is required, which requires more extensive investigation. Such an in depth quantification of loss of signal amplification is the subject of a future study.

For an element not affected by loss of signal amplification, its RSC is mostly dependent on its ion yield at laser ablation. This is visualized in Fig. 6, which shows a dependence of element sensitivity on the Fermi energy [47], a measure for the energy required
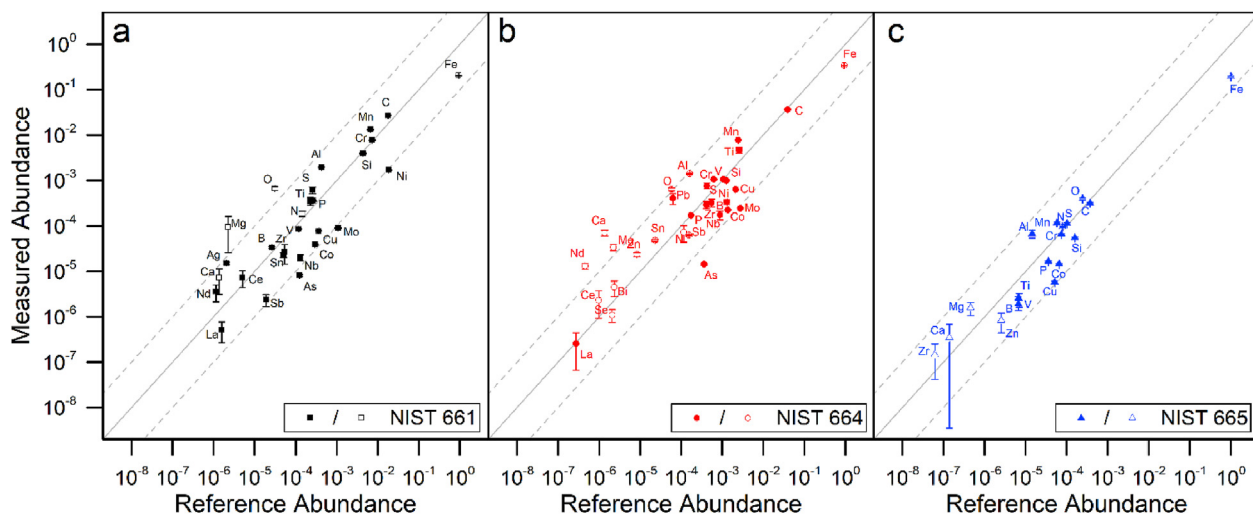
Fig. 4. Measured abundance versus reference abundance specified by NIST for all detected elements for each sample, given in normalized atomic fraction. Each point is the mean of 50 locations analyzed for each sample. The error bars represent the error of the mean. Solid symbols represent certified reference abundances, whereas open symbols represent values reported by a single method. The diagonal lines (dashed and solid) are meant to guide the readers' eye, and indicate the ratio between measured and reference abundance of 1:1, 1:10, and 10:1, respectively. Tables containing the values for each element can be found in the Supplementary Information.
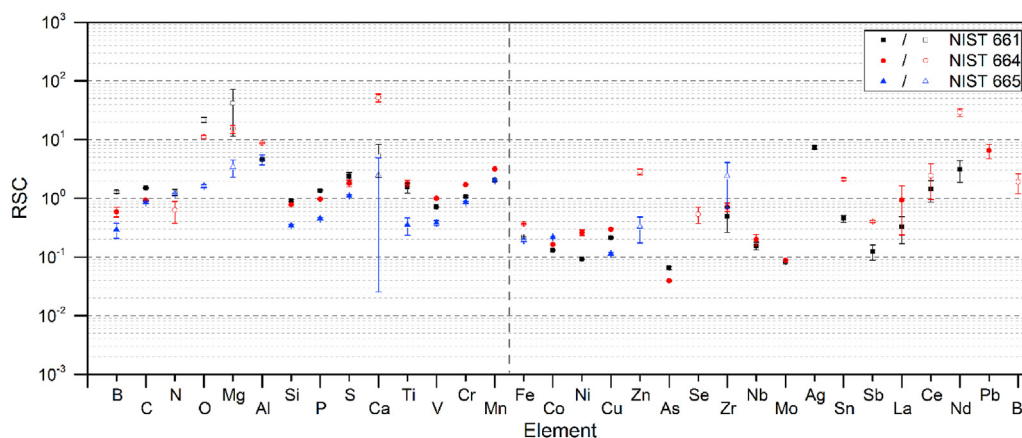
Fig. 5. Calculated relative sensitivity coefficients for all detected elements per sample. The dashed line is meant to guide the readers' eye, and separates those elements unaffected by loss of detection efficiency in the detector (left) from those affected by it (right). Solid symbols represent certified reference abundances, whereas open symbols represent values reported by a single value. Tables containing the values for each element can be found in the Supplementary Information.

to promote an electron at or near the surface into the conduction band, causing charge separation which is at the root of the fs laser ablation process. As shown previously, the RSCs for a given element correlate with variations in ablation and ionization efficiencies in LIMS [48]. Since RSCs of elements heavier than Fe suffer from detector loss of signal amplification, they are not taken into account in Fig. 6. For elements lighter than Fe, a downward trend of the RSCs with increasing Fermi energy can be observed. Aluminum clearly deviates slightly from this trend, which might be due to a contamination of the sample with aluminum oxides leftover from the polishing procedure, which would result in a higher signal for Al, and consequently a high apparent RSC.

Another possible factor in variating relative sensitivities is surface oxidation. However, surface oxidation is not expected to play a role in the observed variation of RSCs. Firstly, the short time between the polishing sample preparation and measurement (in the order of several hours) is not expected have been sufficient for the build-up of a significant oxidation layer. Secondly, thin oxidation layers that did form were not taken into account for RSC calculation, since the first 100 layers of ablated material were excluded from analysis. Past this point any oxidation layer that might have formed

is expected to already be removed by the previous laser shots.

An additional source of the large range in element sensitivities in the current LMS-GT setup is the use of IR irradiation. Due to the lower photon energy of IR photons, multi-photon events are required for ionization of elements with a high ionization energy level. The increased energy of UV photons results in less multi-photon events being required to ionize different elements, which results in a more stoichiometric plasma, which, in turn, results in a smaller range in RSCs [46,49,50]. However, while there are different sensitivities for different elements with the current setup, which can be accounted for by the derived RSCs, the use of a fs IR laser ablation source is still expected to yield a smaller range in relative sensitivities (by orders of magnitude) compared to employing a ns pulsed laser system as ion source for LMS-GT. Nanosecond laser pulses are known to cause severe fractionation due to interaction of the laser pulse tail with the plasma of the expanding ablation plume as well as due to thermal effects causing melting and significant sample damage [20,26].

Distribution of elements throughout the material. While it is stated in the certificate of analysis provided by NIST for each of the characterized SRM samples that the materials were produced to
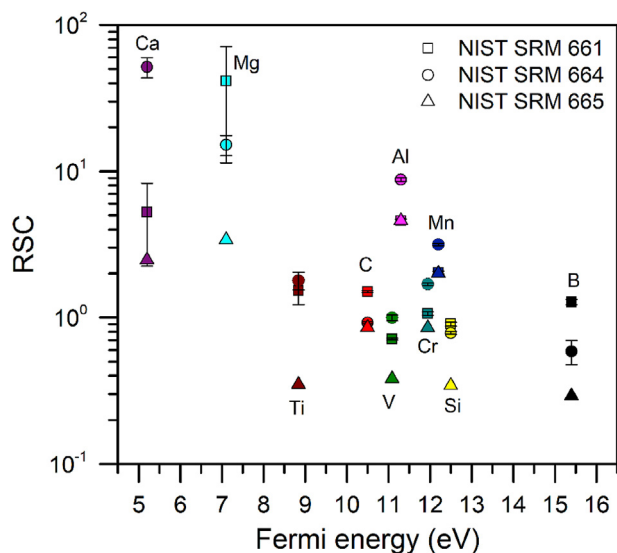
Fig. 6. Dependence of the relative sensitivity coefficient on the Fermi Energy for each element detected before Fe in the different samples. Each point is the average of 50 analyzed locations per sample. Fermi energies taken from Halas et al. (1998) [47].

achieve the highest level of homogeneity in the distribution of elements, perfect homogeneity at the micrometer scale cannot be guaranteed. In fact, compositional heterogeneities are known to exist within each of the samples [51]. The high spatial resolving power of LMS-GT allows not only to conduct bulk-like chemical analysis by averaging values obtained from multiple sample locations but also allows for information on the distribution of elements throughout the sample material to be acquired.

Fig. 7 shows the location-to-location variation of abundances corrected by their RSCs calculated for selected elements of NIST SRM 661. As can be seen, not all elements are distributed similarly.
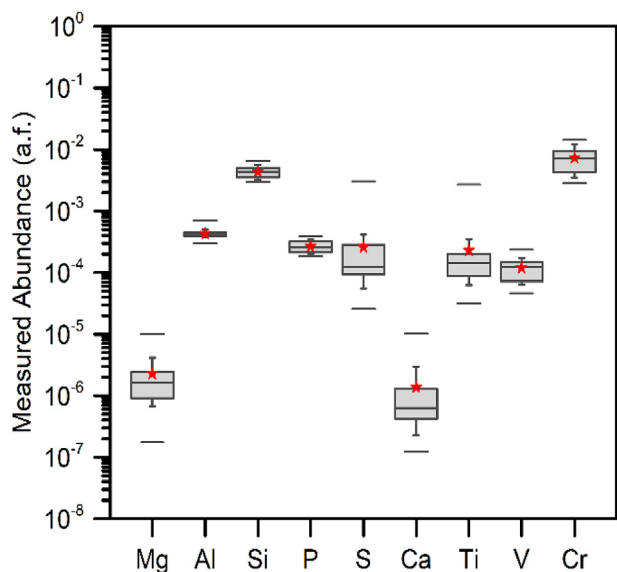
Fig. 7. Location-to-location variation of the RSC-corrected abundance of selected elements in NIST SRM 661. The middle line of each box represents the median value of all 50 locations. Boundaries of the box are 25% and 75%, while for the bars, the boundaries are 10% and 90%. The floating lines represent the minimum and maximum recorded value. The red stars represent the reference abundance as stated by NIST.

While elements such as Al, Si, and P were found to be rather evenly distributed throughout the material, others (e.g., Mg, S, and Ca) showed large variations exceeding a full order of magnitude between lowest and highest recorded intensities. As several elements, including Mg, S, and Ti, are known to display a low solid solubility and high segregation coefficient in Fe, the segregation of elements suggested by the observed level of variation is in line with expectations [52—54].

For Mg and Ca, the relatively high fluctuation can be partly attributed to their abundances being close to the detection limit, which increases the effect of random noise on the area under the peak. However, S and Ti are present at levels well above the detection limit, minimizing the effect of random noise. As a result, the variation in signal intensity for these elements can most confidently be attributed to local variation in their relative abundance. The high level of variation observed for these elements demonstrates the necessity of analyzing a sufficiently large volume of material when aiming to calculate RSCs for accurate quantification of these SRM materials since the certified element abundances are bulk values.

Dependence of relative sensitivities on instrument parameters. An additional measurement campaign was conducted to investigate the dependence of the observed RSC values on several parameters. Matrix dependence of the obtained RSC values was assessed through measurements conducted on BCS-SRM 180/2, a Cu—Ni alloy material provided by BAS. The influence of varying pulse energy was investigated by applying a range of pulse energies on this same sample. The results of the campaign are shown in Fig. 8. Fig. 8a shows a similar trend as can be observed in Fig. 4: the majority of elements plot along the diagonal line, meaning the measured abundance matches the reference abundance relatively well, while some elements (Mn and S) show slight deviations. Moreover, none of the elements in Fig. 9 show a large variation in RSC value with the applied laser power. In other words, no dependence of RSC on applied laser power was observed in the selected range. Note that the range of laser powers was selected based on spectral properties of the acquired mass spectra; at pulse energies below 0.4 μJ, little-to-no signal was observed, while at pulse energies above 1.13 μJ, both detector gain loss and significant peak broadening due to space charge effects started to occur. This is again exemplified more quantitatively in Table 2, where RSC scores for the different laser energies are listed. RSC scores were calculated according to the following formula:

$$RSC\ score = \left(1 - \left(\frac{1}{x}\sum_{1}^{x}\frac{|1 - RSC_x|}{1 + RSC_x}\right)\right)*100\%$$

where x represents the number of elements being taken into account, which allows different sets of RSC values to be compared. As can be seen in Table 2, where no significant improvements in RSC scores are observed for any of the applied pulse energies.

Fig. 9c shows the obtained RSC values for all four investigated samples for those elements that are certified in all four. For most elements, the measured RSC value (Fig. 9b) differs from that measured for the NIST SRM steel samples by a factor 2—8, when applying the same laser power (0.57 μJ). This dependence of RSC values on the matrix indicates that LMS-GT, when operated at IR laser wavelengths, shows some matrix effects, which is in line with expectations due to the inherent matrix dependence of the laser ablation ionization process [20,28]. However, the same S-shape trend can be recognized for all four samples, which indicates that some factor which influences RSC values is applicable in all investigated materials. Note that the RSC value for Cu, the main constituent of BCS-CRM 180/2, is roughly equal to one, which is in
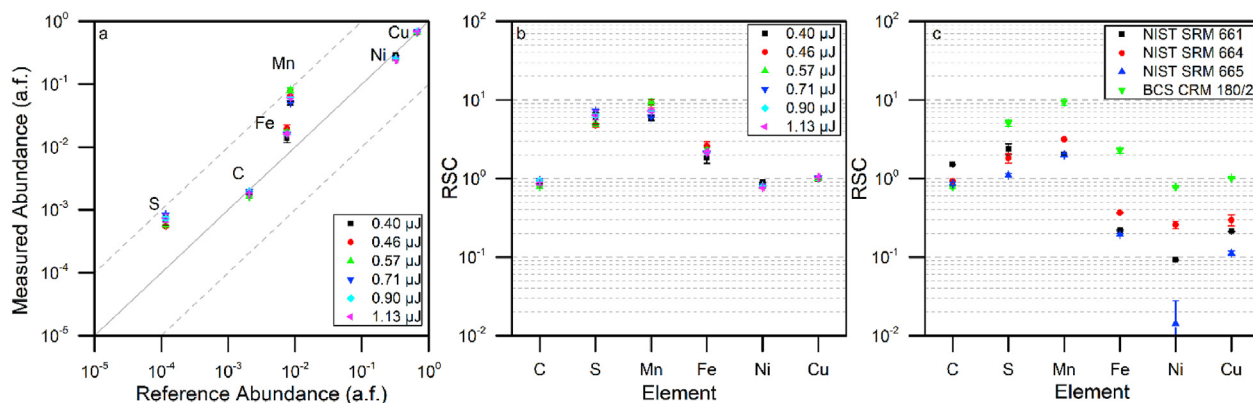
Fig. 8. Dependence of observed relative sensitivity on applied pulse energy, measured on BCS-SRM 180/2 (see the supplementary information for the values). a) Measured abundance versus reference abundance specified by BAS for all elements, given in normalized atomic fraction. The error bars represent the error of the mean. The diagonal lines (dashed and solid) are meant to guide the readers' eye, and show the lines points would lie on if the ratio between measured and reference abundance is 1:1, 1:10, or 10:1. b) Relative sensitivity coefficients for all certified elements. Error bars represent the error of the mean. c) Relative sensitivity coefficients obtained from the investigated NIST and BCS materials for those elements which are certified in all four. The applied pulse energy is 0.57 µJ for all four materials.

Table 2
RSC scores for the campaign to investigate RSC dependence on applied detector voltage. The applied laser pulse energy was 1 µJ after transmission losses.

Applied pulse energy	RSC score
0.40 µJ	70%
0.46 µJ	65%
0.57 µJ	65%
0.71 µJ	67%
0.90 µJ	67%
1.13 µJ	65%

sharp contrast with the RSC values obtained for Fe in the NIST steel sample investigations. Indeed, the Cu abundance in BCS-CRM 180/2 is certified, whereas the Fe abundance in the NIST steel samples is not, which exemplifies the importance of only considering elements with certified abundances for RSC determinations.

4. Conclusion and outlook

A detailed study on three NIST SRM steel samples was conducted to assess the quantitative capabilities of the LMS-GT high mass resolution LIMS system. The achieved maximum mass resolution of 12,000, measured at m/z 90, is a ~10% enhancement with respect to our previous study, most likely due to optimization in applied laser power [41]. The combination of high mass resolution, sub-ppm detection sensitivity, and high achievable spatial resolution makes LMS-GT a promising analytical tool for the chemical analysis of solids.

A major advantage of its high mass resolution lies in the large reduction of the number of peaks affected by isobaric interferences. This facilitates identification while simultaneously allowing for quantification of peaks that would have been unresolvable at a lower mass resolution. The high mass accuracy enables confident species identification, which is especially valuable in cases where isotope patterns cannot be used.

Calculated RSC values show a definitive loss of signal amplification after a highly intense peak (in this case Fe) as a result of detector gain loss. For the majority of elements unaffected by loss of signal amplification, RSC values were calculated to lie between 0.5 and 5, which is in line with expected values based on results achieved with other LIMS systems. However, several elements suffer

from relative sensitivities exceeding one order of magnitude, such as Mg, Ca, and Pb. No significant dependence of relative sensitivities on applied laser power was observed, indicating a certain robustness of the applied measurement technique. The expected matrix dependence was observed, with most elements displaying a factor 2−8 difference between a steel matrix and a Cu−Ni alloy matrix.

To enhance the quantitative capabilities of LMS-GT, differences in relative sensitivity should be minimized, which would reduce reliance on matrix-matched standards for accurate quantification of the chemical composition of unknown samples. Using IR fs-laser irradiation as an ablation ion source has been shown to induce a larger range in relative sensitivity of species compared to using UV fs-laser irradiation. Consequently, incorporating a UV fs-laser system as an ablation ion source into the current measurement setup is expected to bring RSC values closer to one, although some dependence on material-specific properties is always to be expected.

As is, the LMS-GT LIMS system shows potential as a versatile analytical tool for the chemical analysis of solids, with a wide range of scientific and industrial applications. Its lateral resolution at the micrometer scale, low detection limits at the ppb level, and high mass resolution that allows resolving isobaric interferences constitute an interesting set of analytical capabilities. These specific capabilities could be especially advantageous during, e.g., *in situ* chemical analysis of microscale inclusions in geological and meteoritic samples, as well as investigation of microscale inhomogeneity/incorporations in deposited materials such as coatings or semiconductor components. However, further development on the ablation ion source and mass analyzer is required to further improve its quantitative performance.

Credit author statement

C.P. de Koning, Conceptualization, Software, Formal analysis, Investigation, Validation, Writing − Original draft, Writing − Review&Editing, Visualization: S. Gruchola, Conceptualization, Investigation, Writing − Review & Editing: A. Riedo, Writing − Review & Editing, ConceptualizationR. Wiesendanger, Methodology: V. Grimaudo, Writing − Review & Editing, Conceptualization; R. Lukmanov, Writing − Review & Editing: N.F.W. Ligterink, Writing − Review & Editing: M. Tulej, Writing − Review & Editing, Supervision: P. Wurz, Writing − Review & Editing, Supervision, Funding acquisition, Project Administration, Resources.

Declaration of competing interest

The authors declare that they have no known competing financial interests or personal relationships that could have appeared to influence the work reported in this paper.

Acknowledgements

Appendix A. Supplementary data

Supplementary data to this article can be found online at https://doi.org/10.1016/j.ijms.2021.116662.

References

[1] H.M. Ortner, P. Wilhartitz, Ultratrace and microdistribution analysis in material sciences, Fresenius' J. Anal. Chem. 337 (1990) 686–700, https://doi.org/10.1007/BF00323102.

[2] A.K. Knight, N.L. Scherbarth, D.A. Cremers, M.J. Ferris, Characterization of laser-induced breakdown spectroscopy (LIBS) for application to space exploration, Appl. Spectrosc. 54 (2000) 331–340, https://doi.org/10.1366/0003702001949591.

[3] W.B. Brinckerhoff, G.G. Managadze, R.W. McEntire, A.F. Cheng, W.J. Green, Laser time-of-flight mass spectrometry for space, Rev. Sci. Instrum. 71 (2000) 536–545, https://doi.org/10.1063/1.1150237.

[4] M. Golitko, Introduction to solid sampling strategies, in: L. D, M. G, B. G (Eds.), Recent Adv. Laser Ablation ICP-MS Archaeol., Springer Verlag, Berlin, Heidelberg, 2016, pp. 23–25, https://doi.org/10.1007/978-3-662-49894-1_2.

[5] V. Grimaudo, P. Moreno-García, A. Riedo, M.B. Neuland, M. Tulej, P. Broekmann, P. Wurz, High-resolution chemical depth profiling of solid material using a miniature laser ablation/ionization mass spectrometer, Anal. Chem. 87 (2015) 2037–2041, https://doi.org/10.1021/ac504403j.

[6] V. Grimaudo, P. Moreno-García, A. Riedo, S. Meyer, M. Tulej, M.B. Neuland, M. Mohos, C. Gütz, S.R. Waldvogel, P. Wurz, P. Broekmann, Toward three-dimensional chemical imaging of ternary Cu-Sn-Pb alloys using femtosecond laser ablation/ionization mass spectrometry, Anal. Chem. 89 (2017) 1632–1641, https://doi.org/10.1021/acs.analchem.6b03738.

[7] Y. Lin, Q. Yu, W. Hang, B. Huang, Progress of laser ionization mass spectrometry for elemental analysis - a review of the past decade, Spectrochim. Acta Part B At. Spectrosc. 65 (2010) 871–883, https://doi.org/10.1016/j.sab.2010.08.007.

[8] V.A. Azov, L. Mueller, A.A. Makarov, Laser ionization mass spectrometry at 55: quo Vadis? Mass Spectrom. Rev. (2020) https://doi.org/10.1002/mas.21669.

[9] J.S. Becker, H.J. Dietze, Inorganic trace analysis by mass spectrometry, Spectrochim. Acta, Part B At. Spectrosc. 53 (1998) 1475–1506, https://doi.org/10.1016/S0584-8547(98)00110-4.

[10] J.S. Becker, H.J. Dietze, Inorganic mass spectrometric methods for trace, ultratrace, isotope, and surface analysis, Int. J. Mass Spectrom. 197 (2000) 1–35, https://doi.org/10.1016/S1387-3806(99)00246-8.

[11] D.W. Hahn, N. Omenetto, Laser-induced breakdown spectroscopy (LIBS), part II: review of instrumental and methodological approaches to material analysis and applications to different fields, Appl. Spectrosc. 66 (2012) 347–419, https://doi.org/10.1366/11-06574.

[12] A. Limbeck, P. Galler, M. Bonta, G. Bauer, W. Nischkauer, F. Vanhaecke, Recent advances in quantitative LA-ICP-MS analysis: challenges and solutions in the life sciences and environmental chemistry ABC Highlights: authored by Rising Stars and Top Experts, Anal. Bioanal. Chem. 407 (2015) 6593–6617, https://doi.org/10.1007/s00216-015-8858-0.

[13] J. Rakovský, P. Čermák, O. Musset, P. Veis, A review of the development of portable laser induced breakdown spectroscopy and its applications, Spectrochim. Acta Part B At. Spectrosc. 101 (2014) 269–287, https://doi.org/10.1016/j.sab.2014.09.015.

[14] D. Günther, B. Hattendorf, Solid sample analysis using laser ablation inductively coupled plasma mass spectrometry, TrAC Trends Anal. Chem. (Reference Ed.) 24 (2005) 255–265, https://doi.org/10.1016/j.trac.2004.11.017.

[15] J. Koch, D. Günther, Laser ablation inductively coupled plasma mass spectrometry, in: Encycl. Spectrosc. Spectrom, Elsevier, 2016, pp. 526–532, https://doi.org/10.1016/B978-0-12-803224-4.00024-8.

[16] F. Poitrasson, F.X. D'Abzac, Femtosecond laser ablation inductively coupled plasma source mass spectrometry for elemental and isotopic analysis: are ultrafast lasers worthwhile? J. Anal. At. Spectrom. 32 (2017) 1075–1091, https://doi.org/10.1039/c7ja00084g.

[17] M. Dong, L. Wei, J.J. González, D. Oropeza, J. Chirinos, X. Mao, J. Lu, R.E. Russo, Coal discrimination analysis using tandem laser-induced breakdown spectroscopy and laser ablation inductively coupled plasma time-of-flight mass spectrometry, Anal. Chem. 92 (2020) 7003–7010, https://doi.org/10.1021/acs.analchem.0c00188.

[18] O. Syta, B. Wagner, E. Bulska, D. Zielińska, G.Z. Żukowska, J. Gonzalez, R. Russo, Elemental imaging of heterogeneous inorganic archaeological samples by means of simultaneous laser induced breakdown spectroscopy and laser ablation inductively coupled plasma mass spectrometry measurements, Talanta 179 (2018) 784–791, https://doi.org/10.1016/j.talanta.2017.12.011.

[19] M. Bonta, J.J. Gonzalez, C. Derrick Quarles, R.E. Russo, B. Hegedus, A. Limbeck, Elemental mapping of biological samples by the combined use of LIBS and LA-ICP-MS, J. Anal. At. Spectrom. 31 (2016) 252–258, https://doi.org/10.1039/c5ja00287g.

[20] A. Riedo, M. Neuland, S. Meyer, M. Tulej, P. Wurz, Coupling of LMS with a fs-laser ablation ion source: elemental and isotope composition measurements, J. Anal. At. Spectrom. 28 (2013) 1256–1269, https://doi.org/10.1039/c3ja50117e.

[21] V. Grimaudo, M. Tulej, A. Riedo, R. Lukmanov, N.F.W. Ligterink, C. de Koning, P. Wurz, UV post-ionization laser ablation ionization mass spectrometry for improved nm-depth profiling resolution on Cr/Ni reference standard, Rapid Commun. Mass Spectrom. 34 (2020) e8803, https://doi.org/10.1002/rcm.8803.

[22] J. Wang, Z. Wang, F. Liu, L. Cai, J. Bin Pan, Z. Li, S. Zhang, H.Y. Chen, X. Zhang, Y. Mo, Vacuum ultraviolet laser desorption/ionization mass spectrometry imaging of single cells with submicron craters, Anal. Chem. 90 (2018) 10009–10015, https://doi.org/10.1021/acs.analchem.8b02478.

[23] T. Green, I. Kuznetsov, D. Willingham, B.E. Naes, G.C. Eiden, Z. Zhu, W. Chao, J.J. Rocca, C.S. Menoni, A.M. Duffin, Characterization of extreme ultraviolet laser ablation mass spectrometry for actinide trace analysis and nanoscale isotopic imaging, J. Anal. At. Spectrom. 32 (2017) 1092–1100, https://doi.org/10.1039/c7ja00088j.

[24] Q. Yu, R. Huang, L. Li, L. Lin, W. Hang, J. He, B. Huang, Applicability of standardless semiquantitative analysis of solids by high-irradiance laser ionization orthogonal time-of-fight mass spectrometry, Anal. Chem. 81 (2009) 4343–4348, https://doi.org/10.1021/ac900141z.

[25] A.A. Sysoev, A.A. Sysoev, Can laser-ionisation time-of-flight mass spectrometry be a promising alternative to laser ablation/inductively-coupled plasma mass spectrometry and glow discharge mass spectrometry for the elemental analysis of solids? Eur. J. Mass Spectrom. 8 (2002) 213–232, https://doi.org/10.1255/ejms.494.

[26] B. Zhang, M. He, W. Hang, B. Huang, Minimizing matrix effect by femtosecond laser ablation and ionization in elemental determination, Anal. Chem. 85 (2013) 4507–4511, https://doi.org/10.1021/ac400072j.

[27] M. Tulej, R. Wiesendanger, A. Riedo, G. Knopp, P. Wurz, Mass spectrometric analysis of the Mg plasma produced by double-pulse femtosecond laser irradiation, J. Anal. At. Spectrom. 33 (2018) 1292–1303, https://doi.org/10.1039/c8ja00036k.

[28] A. Riedo, A. Bieler, M. Neuland, M. Tulej, P. Wurz, Performance evaluation of a miniature laser ablation time-of-flight mass spectrometer designed for in situ investigations in planetary space research, J. Mass Spectrom. 48 (2013) 1–15, https://doi.org/10.1002/jms.3104.

[29] G.L. Klunder, P.M. Gran, B.D. Andresen, R.E. Russo, Direct chemical analysis of solids by laser ablation in an ion storage time-of-flight mass spectrometer, Anal. Chem. 76 (2004) 1249–1256, https://doi.org/10.1021/ac0303261.

[30] A.A. Sysoev, Time-of-flight analysers with sector fields: advances and prospects, Eur. J. Mass Spectrom. 6 (2000) 501–513, https://doi.org/10.1255/ejms.380.

[31] R. Huang, Q. Yu, L. Li, Y. Lin, W. Hang, J. He, B. Huang, High irradiance laser ionization orthogonal time-of-flight mass spectrometry: a versatile tool for solid analysis, Mass Spectrom. Rev. 30 (2011) 1256–1268, https://doi.org/10.1002/mas.20331.

[32] T. Stephan, R. Trappitsch, A.M. Davis, M.J. Pellin, D. Rost, M.R. Savina, R. Yokochi, N. Liu, CHILI — the Chicago Instrument for Laser Ionization — a new tool for isotope measurements in cosmochemistry, Int. J. Mass Spectrom. 407 (2016) 1–15, https://doi.org/10.1016/j.ijms.2016.06.001.

[33] Q. Yu, L. Chen, R. Huang, W. Hang, B. Huang, W. Hang, J. He, Laser ionization time-of-flight mass spectrometry for direct elemental analysis, TrAC Trends Anal. Chem. (Reference Ed.) 28 (2009) 1174–1185, https://doi.org/10.1016/j.trac.2009.07.006.

[34] L. Selliez, C. Briois, N. Carrasco, L. Thirkell, R. Thissen, M. Ito, F.R. Orthous-Daunay, G. Chalumeau, F. Colin, H. Cottin, C. Engrand, L. Flandinet, N. Fray, B. Gaubicher, N. Grand, J.P. Lebreton, A. Makarov, S. Ruocco, C. Szopa, V. Vuitton, P. Zapf, Identification of organic molecules with a laboratory prototype based on the Laser Ablation-CosmOrbitrap, Planet. Space Sci. 170 (2019) 42–51, https://doi.org/10.1016/j.pss.2019.03.003.

[35] C. Briois, R. Thissen, L. Thirkell, K. Aradj, A. Bouabdellah, A. Boukrara, N. Carrasco, G. Chalumeau, O. Chapelon, F. Colin, P. Coll, H. Cottin, C. Engrand, N. Grand, J.P. Lebreton, F.R. Orthous-Daunay, C. Pennanech, C. Szopa, V. Vuitton, P. Zapf, A. Makarov, Orbitrap mass analyser for in situ characterisation of planetary environments: performance evaluation of a laboratory prototype, Planet. Space Sci. 131 (2016) 33–45, https://doi.org/10.1016/j.pss.2016.06.012.

[36] R. Arevalo, L. Selliez, C. Briois, N. Carrasco, L. Thirkell, B. Cherville, F. Colin, B. Gaubicher, B. Farcy, X. Li, A. Makarov, An Orbitrap-based laser desorption/ablation mass spectrometer designed for spaceflight, Rapid Commun. Mass Spectrom. 32 (2018) 1875–1886, https://doi.org/10.1002/rcm.8244.

[37] D. Grinfeld, H. Stewart, M. Skoblin, E. Denisov, M. Monastyrsky, A. Makarov, Space-charge dynamics in Orbitrap mass spectrometers, Int. J. Mod. Phys. 34

(2019) 1–15, https://doi.org/10.1142/S0217751X19420077.

[38] M.L. Easterling, T.H. Mize, I.J. Amster, MALDI FTMS analysis of polymers: improved performance using an open ended cylindrical analyzer cell, Int. J. Mass Spectrom. Ion Process. 169–170 (1997) 387–400, https://doi.org/10.1016/s0168-1176(97)00229-2.

[39] F. Aubriet, V. Carré, Fourier transform ion cyclotron resonance mass spectrometry and laser: a versatile tool. https://doi.org/10.1016/B978-0-12-814013-0.00010-7, 2019.

[40] S. Jeong, K.J. Fisher, R.F. Howe, G.D. Willett, Laser ablation Fourier transform mass spectrometric study of zeolites, Microporous Mater. 4 (1995) 467–473, https://doi.org/10.1016/0927-6513(95)00025-5.

[41] R. Wiesendanger, V. Grimaudo, M. Tulej, A. Riedo, R. Lukmanov, N. Ligterink, R. Fausch, H. Shea, P. Wurz, The LMS-GT instrument-a new perspective for quantification with the LIMS-TOF measurement technique, J. Anal. At. Spectrom. 34 (2019) 2061–2073, https://doi.org/10.1039/c9ja00235a.

[42] S. Meyer, A. Riedo, M.B. Neuland, M. Tulej, P. Wurz, Fully automatic and precise data analysis developed for time-of-flight mass spectrometry, J. Mass Spectrom. 52 (2017) 580–590, https://doi.org/10.1002/jms.3964.

[43] J.S. Becker, Appendix I, in: Inorg. Mass Spectrom. Princ. Appl, Wiley & Sons, Ltd., 2007, pp. 463–469, https://doi.org/10.4159/harvard.9780674733527.c26.

[44] V. Možná, J. Pisonero, M. Holá, V. Kanický, D. Günther, Quantitative analysis of Fe-based samples using ultraviolet nanosecond and femtosecond laser ablation-ICP-MS, J. Anal. At. Spectrom. 21 (2006) 1194–1201, https://doi.org/10.1039/b606988f.

[45] C.C. Garcia, H. Lindner, A. Von Bohlen, C. Vadla, K. Niemax, Elemental fractionation and stoichiometric sampling in femtosecond laser ablation, J. Anal. At. Spectrom. 23 (2008) 470–478, https://doi.org/10.1039/b718845e.

[46] R.E. Russo, X. Mao, J.J. Gonzalez, S.S. Mao, Femtosecond laser ablation ICP-MS, in: J. Anal. At. Spectrom, The Royal Society of Chemistry, 2002, pp. 1072–1075, https://doi.org/10.1039/b202044k.

[47] S. Halas, T. Durakiewicz, Work functions of elements expressed in terms of the Fermi energy and the density of free electrons, J. Phys. Condens. Matter 10 (1998) 10815–10826, https://doi.org/10.1088/0953-8984/10/48/005.

[48] M.B. Neuland, V. Grimaudo, K. Mezger, P. Moreno-García, A. Riedo, M. Tulej, P. Wurz, Quantitative measurement of the chemical composition of geological standards with a miniature laser ablation/ionization mass spectrometer designed for in situ application in space research, Meas. Sci. Technol. 27 (2016), 035904, https://doi.org/10.1088/0957-0233/27/3/035904.

[49] J.J. Gonzalez, A. Fernandez, D. Oropeza, X. Mao, R.E. Russo, Femtosecond laser ablation: experimental study of the repetition rate influence on inductively coupled plasma mass spectrometry performance, Spectrochim. Acta Part B At. Spectrosc. 63 (2008) 277–286, https://doi.org/10.1016/j.sab.2007.11.035.

[50] J. González, S.H. Dundas, C.Y. Liu, X. Mao, R.E. Russo, UV-femtosecond and nanosecond laser ablation-ICP-MS: internal and external repeatability, J. Anal. At. Spectrom. 21 (2006) 778–784, https://doi.org/10.1039/b603492f.

[51] R. Mavrodineanu, R.W. Seward, Standard reference materials:, gaithersburg, MD. https://doi.org/10.6028/NBS.SP.260-71, 1981.

[52] C.J. McMahon, L. Marchut, Solute segregation in iron-based alloys, J. Vac. Sci. Technol. 15 (1978) 450–466, https://doi.org/10.1116/1.569592.

[53] T.B. Massalski, Structure and stability of alloys, in: R.W. Cahn, P. Haasen (Eds.), Phys. Metall., 4th ed., Elsevier, 1996, pp. 135–204, https://doi.org/10.1016/B978-044489875-3/50007-7.

[54] T. Rosenqvist, B.L. Dunicz, Solid solubility of sulphur in iron, JOM 4 (1952) 604–608, https://doi.org/10.1007/bf03397727.